ADVANCED FUNCTIONAL MATERIALS
www.afm-journal.de

Bench-Top Fabrication of Hierarchically Structured High-Surface-Area Electrodes

Christine M. Gabardo, Yujie Zhu, Leyla Soleymani, and Jose M. Moran-Mirabal**

Fabrication of hierarchical materials, with highly optimized features from the millimeter to the nanometer scale, is crucial for applications in diverse areas including biosensing, energy storage, photovoltaics, and tissue engineering. In the past, complex material architectures have been achieved using a combination of top-down and bottom-up fabrication approaches. A remaining challenge, however, is the rapid, inexpensive, and simple fabrication of such materials systems using bench-top prototyping methods. To address this challenge, the properties of hierarchically structured electrodes are developed and investigated by combining three bench-top techniques: top-down electrode patterning using vinyl masks created by a computer-aided design (CAD)-driven cutter, thin film micro/nanostructuring using a shrinkable polymer substrate, and tunable electrodeposition of conductive materials. By combining these methods, controllable electrode arrays are created with features in three distinct length scales: 40 μm to 1 mm, 50 nm to 10 μm, and 20 nm to 2 μm. The electrical and electrochemical properties of these electrodes are analyzed and it is demonstrated that they are excellent candidates for next generation low-cost electrochemical and electronic devices.

1. Introduction

Recently, there has been increased interest in fabricating hierarchical materials with morphologies tunable in the micron to nanometer scale. Natural hierarchical materials, optimized over multiple length scales through evolution to answer specific functional demands, have inspired the synthesis of hierarchical materials with unique characteristics unparalleled by bulk materials.[1,2] The properties of such materials can be tuned for specific applications by adjusting the material composition, geometry, and size of the structured features. In photovoltaic and photo-electrochemical energy conversion devices, hierarchically branched nanowires enable considerable improvement in light absorption efficiency due to enhanced surface area and light scattering properties.[3,4] Hierarchical structures have also found wide application as tissue engineering scaffolds because they mimic the multiscale features found in biological niches, which not only offer structural support but also provide the microenvironment needed for cell proliferation.[5–7] In drug delivery, hierarchically structured dendrimers are tuned to provide the required geometry, size, and surface chemical functionality to entrap or transport small drug molecules.[8,9] Similarly, the integration of high surface area hierarchical structures on sensing electrodes dramatically improves the speed and sensitivity of electrochemical biosensors.[10–13] These applications highlight the potential that hierarchically structured materials present in the development of functional devices.

Various methods for the fabrication of hierarchical materials have been developed, such as multilayer photolithography,[14] electron-beam lithography,[15] templated self assembly,[16] and soft lithography.[17] While these methods have been used to create nature-inspired hierarchical materials, they often need to be combined in order to span the entire millimeter to nanometer length scale. As a result, they rely on at least one step that requires a mask, template, or a master that cannot be rapidly fabricated in the laboratory. Thus, it remains a major challenge to develop such materials systems using simple laboratory processes and to implement the entire process, from design to fabrication, in timescales from minutes to hours.

A facile and quick approach has been recently developed to fabricate micro- and nanostructured materials, which takes advantage of the thermal shrinking of pre-stressed polymer films, such as polystyrene (PS),[18] polyolefin (PO),[19] and polyethylene.[5] Printing onto PS substrates and shrinking has been used to generate micropatterned templates, which allowed the fabrication of rounded microfluidic channels with critical dimensions as small as 65 μm.[20] Through this shrinking approach, Fu and collaborators also created uniaxial and biaxial wrinkles on gold-coated PS sheets. They demonstrated that the wrinkle wavelength could be tuned by adjusting the thickness of the metal film.[18] More recently, the shrinking approach has been applied to create micro and nanoscale structures with cross-linked PO thin films, which exhibited larger shrinking ratios (up to 95%) and greater shrinking uniformity than PS

C. M. Gabardo, Prof. L. Soleymani
School of Biomedical Engineering
McMaster University
1280 Main St. West, Hamilton, ON L8S 4M1, Canada
E-mail: soleyml@mcmaster.ca
Y. Zhu, Prof. J. M. Moran-Mirabal
Department of Chemistry and Chemical Biology
McMaster University
1280 Main St. West, Hamilton, ON L8S 4M1, Canada
E-mail: moran-mirabal@mcmaster.ca
Prof. L. Soleymani
Department of Engineering Physics
McMaster University
1280 Main St. West, Hamilton, ON L8S 4M1, Canada

DOI: 10.1002/adfm.201203220

substrates.[5] These shrinking methods offer an attractive route to the fast, easy and inexpensive bench-top fabrication of micro- and nanostructured devices, which can aid in the development of functional microdevices.

Here, we present a method combining millimeter patterning through vinyl masking, micrometer stress-driven wrinkling, and nanometer electrodeposition for the controlled fabrication of electrodes with hierarchical structures spanning multiple length scales. This process offers speed, ease of fabrication and cost-effectiveness in producing micro- and nanostructured surfaces. In addition, we show that electrodes fabricated in this fashion display excellent conductive and electrochemical properties, and can be used to monitor charge transfer and reduction/oxidation reactions. Furthermore, the hierarchically structured electrodes exhibited electroactive surface area enhancements in excess of 1000% when compared to flat electrodes. Altogether these results show that our approach to structuring conductive surfaces produces high surface area electrodes that can be incorporated into a variety of microdevices. This newly developed method could facilitate the design and prototyping of tunable material systems applicable to the fabrication of low-cost biosensing, bioprocessing, tissue engineering and photovoltaic devices.

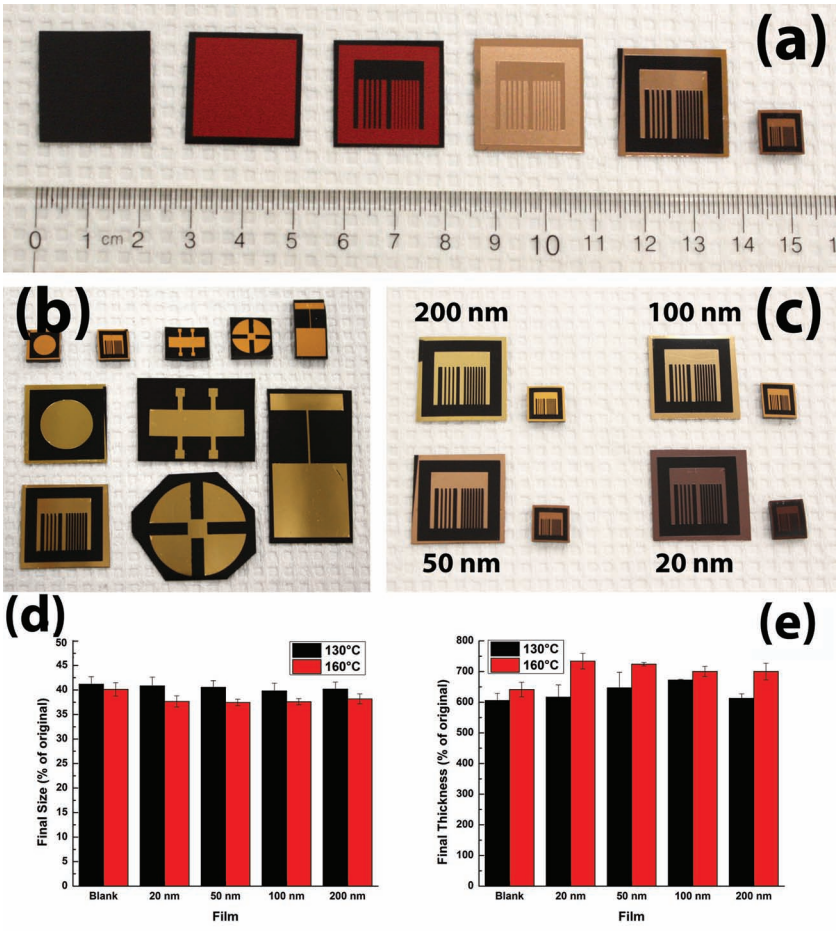

Figure 1. Bench-top fabrication techniques can be used to produce patterned electrodes with critical dimensions <100 µm. a) Depiction of the fabrication of patterned electrodes through vinyl masking and pre-stressed PS substrate shrinking. b) The bench-top approach developed allows the fabrication of patterned electrodes with a wide variety of geometrical shapes. c) Patterned electrodes were fabricated from a variety of gold film thicknesses. Shrinking of the patterned electrodes at 130 and 160 °C was highly reproducible, with d) final transverse dimensions ≈40% of the original size and e) axial dimensions ≈650% of the original size.

2. Results and Discussion

2.1. Quick Prototyping of Patterned Electrodes

Bench-top fabrication techniques offer capabilities to prototype devices in a quick, facile and cost-effective manner. In particular, the ability to rapidly fabricate and test electrodes in a variety of configurations, shapes, and sizes ranging from the millimeter to the micrometer scale, could prove valuable in the development of new sensing electrode architectures for functional devices. To produce patterned electrodes with designed shapes and sizes, we have combined two bench-top fabrication techniques: vinyl film masking and pre-stressed polystyrene (PS) sheet shrinking. The fabrication steps followed to produce patterned thin gold electrodes using the vinyl masking and PS shrinking approach are depicted in **Figure 1**a. Self-adhesive vinyl film was employed as a masking material not only because of its ease of use, ability to bind to a wide range of materials, ease of removal without leaving adhesive residue behind, and adequate resistance to solvents and mild acidic conditions, but also because it can be effectively patterned using a bench-top craft cutter. To produce the pattern masks, self-adhesive vinyl films (red film, Figure 1a) were bound to clean PS sheets (black sheet, Figure 1a) and flattened using a roller. Patterns designed in a computer-aided design (CAD) program were then scored into the vinyl film bound to the PS sheets using a craft cutter. The optimization of the force, speed and acceleration with which the blade cut into the vinyl film allowed us to obtain parallel line cuts with spacings as small as 100 µm (limited by the step size of the cutter motor) and circular features with diameters as small as 200 µm (limited by the turning radius of the blade). The optimized parameters also ensured that the blade did not cut into the underlying PS sheet, which would introduce undesired topography in the final electrodes. The cut out vinyl was peeled-off using rounded tip tweezers to avoid scratching the underlying PS surface. Peeling the vinyl with a uniform force applied parallel to the thinnest features prevented tearing of the vinyl and ensured that it was removed as a continuous film. Once the desired pattern was exposed, a thin gold coating of controlled thickness (20–200 nm) was sputtered onto the devices. Finally, the remaining vinyl mask was lifted-off to reveal a patterned electrode on the PS sheet (Figure 1a).

Occasional tearing, similar to that obtained in resist lift-off processes, could be observed after the vinyl lift-off in SEM images taken from the edges of thick gold films (Supporting Information Figure 1). This patterning approach allowed us to quickly produce electrodes with various shapes and sizes (Figure 1b) and with different film thicknesses (Figure 1c). Although for this study we report on the patterning of gold films, the same approach can be used to produce patterns of a number of different conducive, semiconductive and insulating thin films.

The size of the gold patterns was reduced through biaxial shrinking of the PS substrate to generate electrodes with features as small as 80 μm. When heated above their glass transition temperature of 100 °C,[21] pre-stressed PS sheets have the ability to shrink to under 50% of their original size due to polymer chain relaxation. We have taken advantage of this effect to reduce the dimensions of the features on our patterned gold films. PS sheets containing patterned gold films of thicknesses ranging from 20 to 200 nm were heated at 130 and 160 °C and their shrinking behaviors were characterized. The higher temperature shrunk the devices significantly faster (full shrinking in 2 min) than the lower one (full shrinking in 10 min). It was observed that at both temperatures the shrunken PS sheets and the patterned gold films retained their original overall shape and that shrinking was highly reproducible (Figure 1c) if heat transfer to the PS sheet was uniform. Yet, slight differences were noted between the devices shrunken at the two temperatures. It was noted that devices shrunk at 160 °C reached transverse dimensions that were ≈38% of the original size, while those shrunk at 130 °C only reached ≈40% (Figure 1d). Conversely, the devices shrunk at 160 °C reached ≈700% of their original thickness, while those shrunk at 130 °C reached only ≈650% of their original value (Figure 1e). These small differences are most likely due to the higher fluidity of the PS chains at higher temperatures, as well as the more rapid relaxation of the strain in the pre-stressed film during the shrinking process. Finally, it was also observed that the shrinking process induced the gold films to become more firmly attached to the PS substrates, as shrunken films could not be removed from the surface by the scotch tape peeling test (5 successive peels), but they could be partially removed in unshrunken devices. The increase in adhesive strength has been previously observed[24] and is attributed to the fact that at elevated temperatures the shrinking PS surface becomes soft enough to integrate with the metallic film. Thus, the combination of patterning gold films through vinyl masking and shrinking of the underlying PS substrates has enabled us to quickly produce robust gold electrodes with critical dimensions as small as 80 μm in a reproducible fashion.

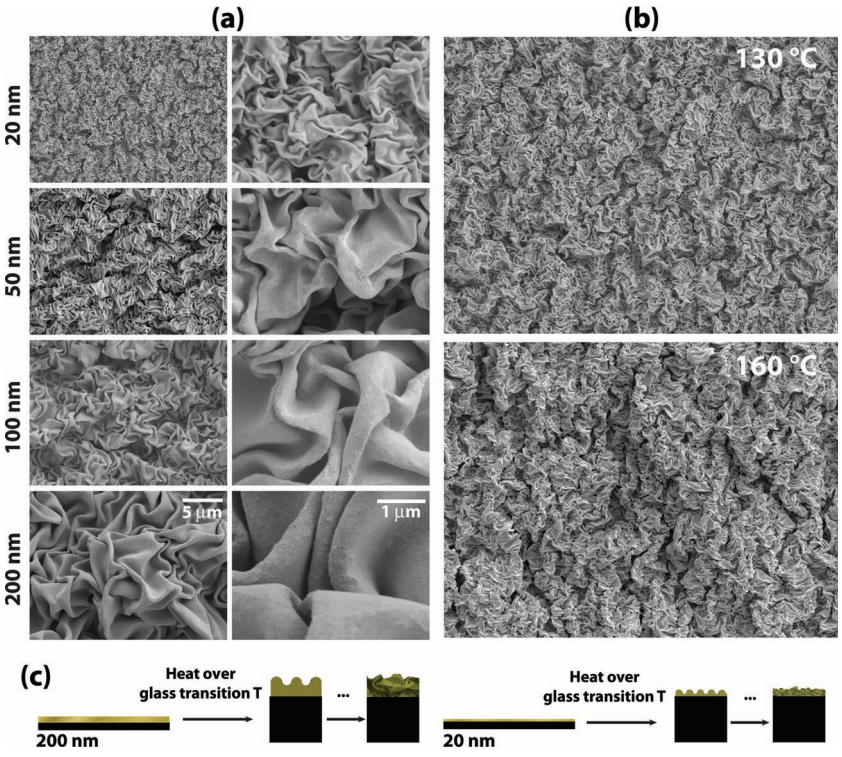

Figure 2. Shrinking of the polystyrene substrate causes an adhered gold film to buckle and wrinkle. a) The size of the resulting wrinkles depends strongly on the film thickness, with thin films resulting in nanoscale wrinkles and thick films resulting in microscale wrinkles. b) The shrinking temperature also affects the wrinkling process, with higher temperatures producing rougher surfaces. c) Schematic depiction of the stress-driven wrinkling of gold films.

2.2. Stress-Driven Micro- and Nanostructuring of Gold Electrodes

In addition to the size-reducing effect, shrinking of the PS substrate induced micro and nanostructuring of the gold film surface. Upon shrinking the patterned gold films, a slight color change appeared and the film became more opaque (Figure 1b,c). Closer inspection revealed that the shrinking process induced texturing on the films, which changed the reflective and scattering properties of the surface, leading to the observed color change. As the PS sheet shrunk, compressive stress was exerted on the pliable gold film and the difference in stiffness between the two materials caused the film to buckle, producing wrinkles ranging from the nanometer to the micrometer scale (**Figure 2**, see Supporting Information Figure 2 for comparison between pristine and shrunken gold films). This effect has been exploited in the past to produce wrinkles in metallic films on polydimethylsiloxane (PDMS),[25,26] on polyethylene sheets,[5] and on thin[27–29] and bulk[18,30] PS substrates. The wrinkling phenomenon has been modeled[31,32] for low shrinking ratios or low compressive stresses and the wavelength of the wrinkles has been estimated to scale as the cube root of the ratio of the elastic moduli of the thin film and the PS substrate multiplied by the film thickness.[33] SEM micrographs of our patterned gold films after shrinking confirmed that the wrinkle size depended strongly on the film thickness, with smaller wrinkles forming on thinner films (Figure 2a). We

observed wrinkled structures that went from the nanometer, for 20 nm thick films, to the micrometer range, for 200 nm thick films. The wrinkles appeared continuous when imaged through electron microscopy, which implied that the patterned gold film was intact. Furthermore, the wrinkles obtained at the large compressive stresses or shrinking ratios obtained from the pre-stressed PS sheets did not appear as regular or ordered as those previously observed from the films undergoing the initial stages of wrinkling instability.[26,27,29] The topologies obtained here had tall hills and deep valleys, which appeared as a result of additional crumpling on top of a first set of wrinkles. A comparison between substrates shrunk at 160 versus 130 °C revealed that the former appeared to have rougher surfaces (Figure 2b). Although the structures observed cannot be modeled by current theoretical descriptions, it is evident that the compressive shrinking rate plays an important role in the second hierarchy of wrinkles. Thus, by controlling the film thickness of the patterned electrodes and the shrinking temperature, structured metallic surfaces with topographical structures that span from the nanometer to the micrometer range were created.

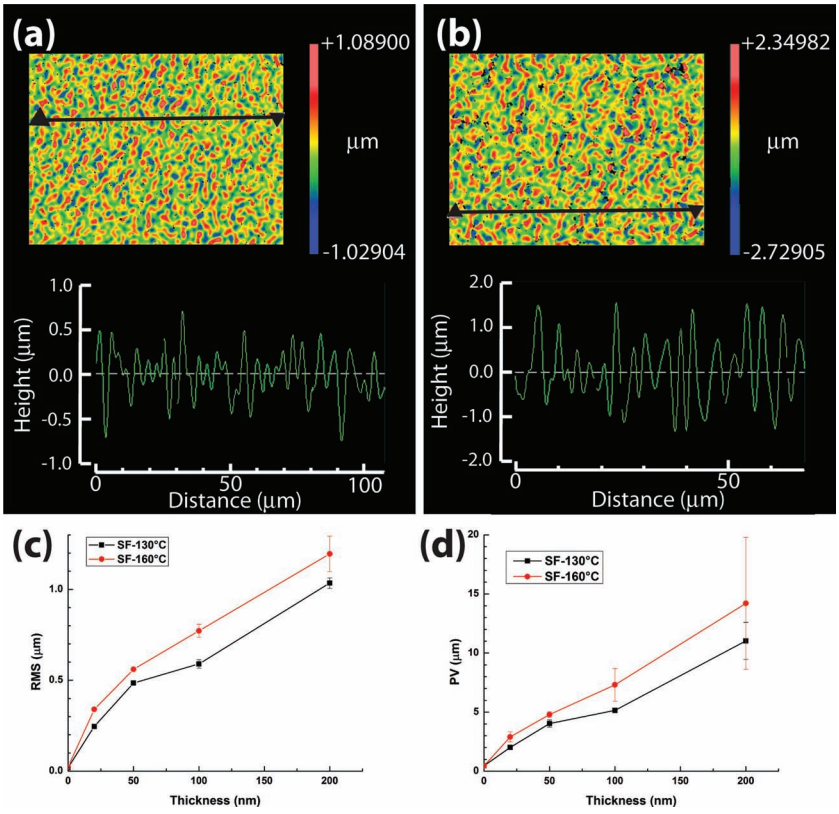

Figure 3. White light interferometry was used to characterize the surface roughness of crumple-structured gold films. a) Sample interferometry image and line profile for a 20 nm thick crumpled film. b) Sample interferometry image and line profile for a 100 nm thick crumpled film. Comparison of c) RMS roughness and d) PV spread for crumple-structured films fabricated at 130 and 160 °C. Error bars represent the standard deviation of replicate measurements performed on the structured films ($n > 3$).

The surfaces of the crumple-structured gold films were characterized through white light interferometry to assess their roughness. Interferometry is a powerful technique that allows the measurement of surface height differences based on fringes, which arise from the interference between a reference and a measuring light beam. The pixel size of the interferometer camera used to image the surfaces was equivalent to 112 nm, which meant that the best lateral resolution that could be achieved was ≈200 nm. While this prevented measuring the nanoscale structure of the thinnest wrinkled films with the same resolution as that of the electron microscope, our measurements revealed significant trends. Interferometry images showed that all crumple-structured films had similar overall surface features with islands of high elevations surrounded by valleys of lower height (**Figure 3**a,b). Although the surface structures looked similar, their heights were significantly different. As figures of merit we chose to characterize the surfaces using their root mean square (RMS) roughness, which indicates the average deviation from the baseline, and the peak-valley spread (PV), which is calculated as the height difference between the highest and the lowest points and reports on the range of height measurements.

All the crumple-structured gold surfaces exhibited RMS surface roughness values that were higher than that of the shrunken PS sheet alone (19 and 23 nm for sheets shrunken at 130 and 160 °C). The RMS roughness for crumple-structured films ranged from 250 nm for 20 nm thick films shrunken at 130 °C, to 1200 nm for 200 nm thick films shrunken at 160° (Figure 3c). The increase in surface roughness was directly correlated with increasing film thickness. This is to be expected, as the thicker films are less pliable and do not buckle as easily during the shrinking step. In addition, we observed that the surface roughness was significantly higher for films shrunken at 160 °C as compared with those shrunken at 130 °C. These differences confirm our observations from SEM images, where the films shrunken at the higher temperature seemed to have deeper valleys and higher peaks. The PV values for crumple-structured films ranged from ~2 µm, for 20 nm films shrunken at 130 °C, to ≈12 µm, for 200 nm films shrunken at 160 °C, and were also significantly higher than those for shrunken PS sheets alone (≈450 nm for films shrunken at both temperatures). The PV followed a similar trend to that observed for the RMS roughness, with increasing PV values for increasing films thickness and higher PV values for films shrunken at 160 °C (Figure 3d). The characterization of the crumple-structured thin films through interferometry demonstrates that the gold electrodes fabricated through vinyl masking and PS sheet shrinking have surfaces that are significantly roughened, and that this surface roughness can be controlled by the choice of film thickness and shrinking temperature.

The increased surface roughness of the micro- and nanostructured films also influenced their wettability. To

characterize the wettability of the patterned gold films we measured the contact angles of water droplets on the films before and after shrinking of the underlying PS substrate (Supporting Information Figure 3). The contact angle of unshrunken gold films of all thicknesses was statistically equal with a value ≈65°, and close to that of unshrunken PS film, which was 70°. Upon shrinking, all the micro- and nanostructured films had increased contact angles, ranging from 104° for 20 nm thick shrunken films, and increasing with thickness to a plateau value close to 120° for 100 and 200 nm thick films. In comparison, the contact angle for the shrunken PS sheets was ≈90°. The increase in contact angle is a direct result of the structured surface and can be understood in terms of the crevices and clefts that are inaccessible to water, resulting in a Cassie or mixed Cassie-Wenzel wetting pattern.[34] These results show that the wettability of gold surfaces can be tailored by controlling the size of the structures induced by the shrinking of the underlying PS substrate. The ability to tailor the wettability of thin film surfaces has attracted much attention, as it can lead to applications such as self-cleaning coatings. The ease with which these structured surfaces are fabricated makes them attractive for the development of multiplexed biosensors and microfluidic devices that exploit the hydrophobic nature of the structured films to integrate multiple samples on a single substrate.

2.3. Electrochemical Characterization of Electrodes Patterned on PS Sheets

Electrical and electronic devices created on polymeric substrates hold great potential in next generation display,[35] chemical and biological sensing,[36] and photovoltaic[37] technologies because their mechanical flexibility and light weight is complemented with rapid and cost-effective manufacturing. In addition, reproducibility in conductivity, electron transfer kinetics, surface area, and electrochemical activity are essential to material systems used in electrochemical sensing. To assess the suitability of metallic films patterned on PS sheets as functional electrodes, we used cyclic voltammetry (CV) to compare the electrochemical behavior of two sets of devices: patterned electrodes on glass substrates and patterned electrodes on unshrunken PS sheets (Supporting Information Figure 4). Self-adhesive vinyl masks with a square cutout were immobilized on the devices to ensure that the electrodes fabricated on glass and PS substrates exposed the same geometric gold surface area (Supporting Information Figure 4a). CV curves of unshrunken PS devices measured in sulfuric acid solutions displayed a well-defined redox signature associated with the oxidation of gold and the subsequent reduction of gold oxide, which compared favorably to the voltammograms obtained from electrodes fabricated on glass (Supporting Information Figure 4b). It was observed that the unshrunken PS devices exhibited a slightly lower electroactive surface area than their glass counterparts exposing the same geometric area, as estimated from the integrated charge contained in the reduction peak of CV scans acquired in H_2SO_4 solutions. We attribute the reduced electroactive surface area to irregularities on the PS substrate surface, which is rougher than the flat polished glass, and to the fabrication conditions where the sputtering of the gold film onto the PS substrates heats the polymer enough that it can partially mix with the metal being deposited. CV curves from PS devices were also obtained in solutions containing the redox complex potassium ferrocyanide. The CV curves taken from unshrunken PS devices exhibited well-defined oxidation and reduction peaks associated with the redox couple ferrocyanide/ferricyanide, which also compared favorably to the voltammograms obtained from devices fabricated on glass (Supporting Information Figure 4c). Analysis of the CV curve characteristics showed that PS devices exhibit redox potentials and peak shapes that closely match those of glass devices and do not display any undesired background electrochemical activity. In addition, PS devices demonstrated exceptional device-to-device reproducibility as the variations in peak potentials and peak currents observed were less than 1% and 8% respectively (Supporting Information Figure 4d). Altogether these experiments show that devices fabricated on PS substrates exhibit electrochemical behavior that closely resembles that of devices fabricated on glass, making them suitable for electrochemical device fabrication.

2.4. Electrical and Electrochemical Properties of Crumple-Structured Electrodes (CSEs)

Tunable high surface area inorganic materials are important to many scientific and industrial applications including catalysis, sensing, separations, and energy storage.[38,39] The ability to fabricate micro- and nanostructured surfaces through benchtop techniques is an attractive route for the rapid development of high surface area electrodes with tunable characteristics. To demonstrate the suitability of CSEs fabricated through benchtop techniques as functional, high surface area electrodes, we conducted a series of measurements of their electrical and electrochemical properties. The continuity and integrity of CSE devices were first evaluated by measuring the sheet resistance of the patterned gold films through the van der Pauw method.[40] The sheet resistance measured for PS devices before shrinking showed decreasing values for increasing gold film thicknesses, with the sheet resistance values tending towards an asymptotic value of 0.28 ohms/square (Supporting Information Figure 5). The sheet resistance for the PS devices after shrinking exhibited a similar trend, with CSEs made from thinner films showing higher sheet resistance than those made with thicker films (Supporting Information Figure 5). In addition, shrunken devices displayed a significantly lower sheet resistance than their unshrunken counterparts. We hypothesize that the decrease in sheet resistance in CSEs arises from the contact between adjacent creases and folds present on the wrinkled films, which yields a shorter path length for current to travel through and results in a lower effective sheet resistance. The observation that the decrease in sheet resistance after shrinking is more significant for thinner films supports this hypothesis, since scanning electron microscopy (SEM) images (Figure 2) show that wrinkles are more closely packed in thinner films and have a higher probability of contacting adjacent structures. The ability to successfully and reproducibly measure sheet resistance values from devices fabricated on PS substrates demonstrates that the gold films before and after shrinking are continuous and suitable for electrical measurements.

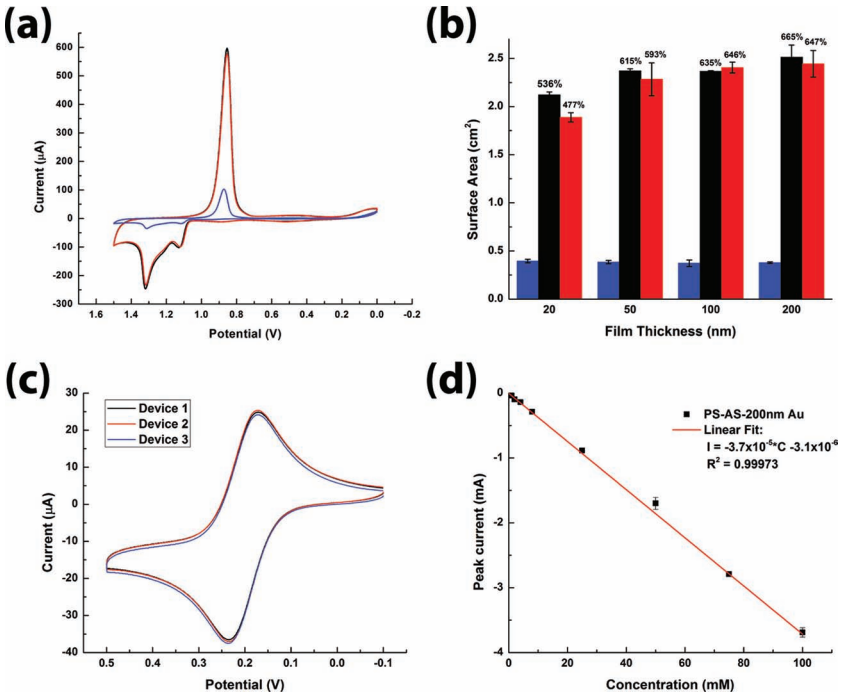

Figure 4. Crumple-structured electrodes are suitable devices for electrochemical measurements. a) A comparison of cyclic voltammograms obtained in dilute acid solutions for electrodes before (blue line) and after shrinking at 130 (black line) and 160 °C (red line). b) Quantification of the charge transferred during the formation of a monolayer of gold oxide reveals significant enhancement of electroactive surface area after shrinking at 130 (black) and 160 °C (red), as compared to that of the unshrunken electrodes (blue). c) Cyclic voltammograms obtained from three different 200 nm CSE devices immersed into a potassium ferrocyanide solution demonstrate the high device-to-device reproducibility. d) Chronoamperometric measurements performed with 200 nm CSEs immersed into solutions containing various concentrations of potassium ferrocyanide demonstrate exceptional linearity in sensing the redox complex.

An attractive feature of the wrinkled topography of CSEs is that these devices could present significantly larger active surfaces per projected geometrical area than flat electrodes. To measure the active surface area of CSEs, we quantified the total charge involved in the electrochemical formation of a monolayer of gold oxide (**Figure 4**a). The active areas of PS devices fabricated with different film thicknesses were compared before and after shrinking at temperatures of 130 and 160 °C (Figure 4a,b). All unshrunken devices, regardless of film thickness, showed the same electroactive surface area, which was expected as no surface structuring is present and all devices present the same geometrical area. On the other hand, all shrunken devices exhibited significantly larger electroactive surface areas, with enhancements as high as 665% of the area presented by unshrunken devices. This result is readily explained, as the shrinking process crumples the original film into a geometrical area that is ≈16% of the original device. Figure 4b also shows that the measured electroactive surface area enhancement for shrunken devices is larger for thicker than for thinner film devices processed using identical methods. This supports our hypothesis that coalescence of adjacent wrinkles is more frequent in CSEs fabricated out of thinner films where the wrinkles are more closely packed. Additionally, we observed that the temperature at which the devices were shrunk could influence the resulting electroactive surface area. Figure 4b shows that shrinking of 20 nm thick devices at 160 °C yielded lower enhancements than shrinking at 130 °C, while the enhancement was not statistically different for all other film thicknesses. This observation can be explained by the faster shrinking kinetics at higher temperature, which results in secondary wrinkles (seen in Figure 2) that leave some of the primary wrinkles inaccessible to the oxidation process. This effect is more pronounced in thin film devices because the wrinkles formed are more closely packed, and are more easily shielded by secondary wrinkling than in thicker film devices. The results from the characterization of the electroactive surface area of CSEs demonstrate that the shrinking process is a facile method to create high surface area electrodes where the surface area enhancement can be tuned through experimental parameters such as film thickness and shrinking temperature.

To investigate the possibility of using high surface area CSEs in electrical and electrochemical devices, we assessed their performance and device-to-device reproducibility in electrochemical measurements. CV measurements were conducted with 200 nm thick CSE devices immersed in a 2 mM solution of potassium ferrocyanide. The CV curves generated from these devices showed peak oxidation/reduction currents and reduction/oxidation potentials (Figure 4c) that compared favorably with those measured from devices fabricated on glass and unshrunken PS substrates (Supporting Information Figure 4c,d). Furthermore, the CV for three CSE devices tested displayed close to identical curves, with variations in peak redox currents and potentials that were <1%. Thus, CSEs are suitable for electrochemical measurements and display an extraordinary device-to-device reproducibility, which translates in highly reliable electrodes for electrochemical device applications. Because electrochemical sensing relies on the accurate and quantifiable detection of redox analytes, we further tested the suitability of CSEs fabricated from 200 nm thick films as electrochemical amperometric sensors. The CSEs were used as working electrodes in a three-electrode electrochemical cell and were used to detect increasing concentrations of potassium ferrocyanide. Chrono-amperometric measurements were used to characterize the electrodes' response to the analyte concentration in solution. Figure 4d shows that the peak current response is linear and highly reproducible for potassium ferrocyanide concentrations in the 50 μM to 100 mM range, which is in accordance with the Cottrell equation for changes in current due to the diffusion limited oxidation of the target analyte. These electrochemical measurements show that CSEs are suitable for the fabrication of electrochemical devices because they exhibit properties that mimic those of electrodes fabricated on traditional substrates, high device-to-device reproducibility, and linearity in sensing of electroactive species. CSEs could thus present an attractive

alternative for the fabrication of highly sensitive electrochemical sensing devices with applications ranging from toxic gas to biomolecular detection.

2.5 Hierarchical Nanostructuring of CSEs through Electrodeposition

Three-dimensional nanostructured electrodes with features in the 10–50 nm range have demonstrated superior sensitivity in detection of biomolecular analytes (e.g., nucleic acids and proteins) than materials comprised of larger grains.[10] In an attempt to develop electrodes suitable for biosensing applications, we sought to bring another level of hierarchical structuring to CSEs through electrodeposition. To this end, gold was electrodeposited from a solution containing $HAuCl_4$ and HCl onto flat electrodes and CSE devices fabricated out of 50 nm thick gold films. Our hypothesis was that the folds and creases present on the CSEs would present regions of local electric field enhancement where electrodeposition would occur preferentially. The resulting nanostructures would increase the electrode surface area, making CSEs even more sensitive and suitable for biosensing applications.

Systematic sampling of the electrodeposition parameter space, allowed the controlled formation of sub-50 nm structures on patterned electrode surfaces. Electrodeposition tests were performed on unshrunken devices to compare the effect of variations in the applied potential and in the concentration of $HAuCl_4$ on the shape and size of the electrodeposited gold structures. SEM images of electrodeposition on flat, unshrunken electrodes (**Figure 5**a) show that as the cathodic potential is decreased from –0.2 to –0.3 V, the resulting electrodeposited gold structures shift from hemispherical and cylindrical grains to 2D leaf-like structures, where the leaf's plane lies perpendicular to the electrode. This difference in grain morphology can be explained as a shift from kinetically-controlled to diffusion-controlled electrodeposition. Previously, the electrodeposition of gold has been categorized as: kinetically controlled at small nucleation overpotentials, mixed kinetically/diffusion controlled at moderate nucleation overpotentials, and diffusion controlled at large nucleation overpotentials.[41] Images of electrodes where the deposition was performed at –0.2 V show hemispherical structures, which are indicative of the radial transport of metal ions associated with mixed kinetically-diffusion controlled electrodeposition. On the other hand, for samples where electrodeposition was performed at –0.3 V the faster reaction kinetics shifted the deposition towards a diffusion-limited regime, where growth instabilities resulted in the formation of irregularly shaped vertical dendrites that coalesced into leaf-like structures as they grew. Furthermore, increasing the concentration of $HAuCl_4$ translated into an increased deposition rate (Supporting Information Figure 6), which increased the size of the structures. However, changing the $HAuCl_4$ concentration did not affect the morphology of the deposited structures.

Having established specific electrodeposition parameters for precisely tuning the size and morphology of the deposited structures on flat electrodes, we proceeded to use these conditions to integrate nanostructured morphologies onto CSE

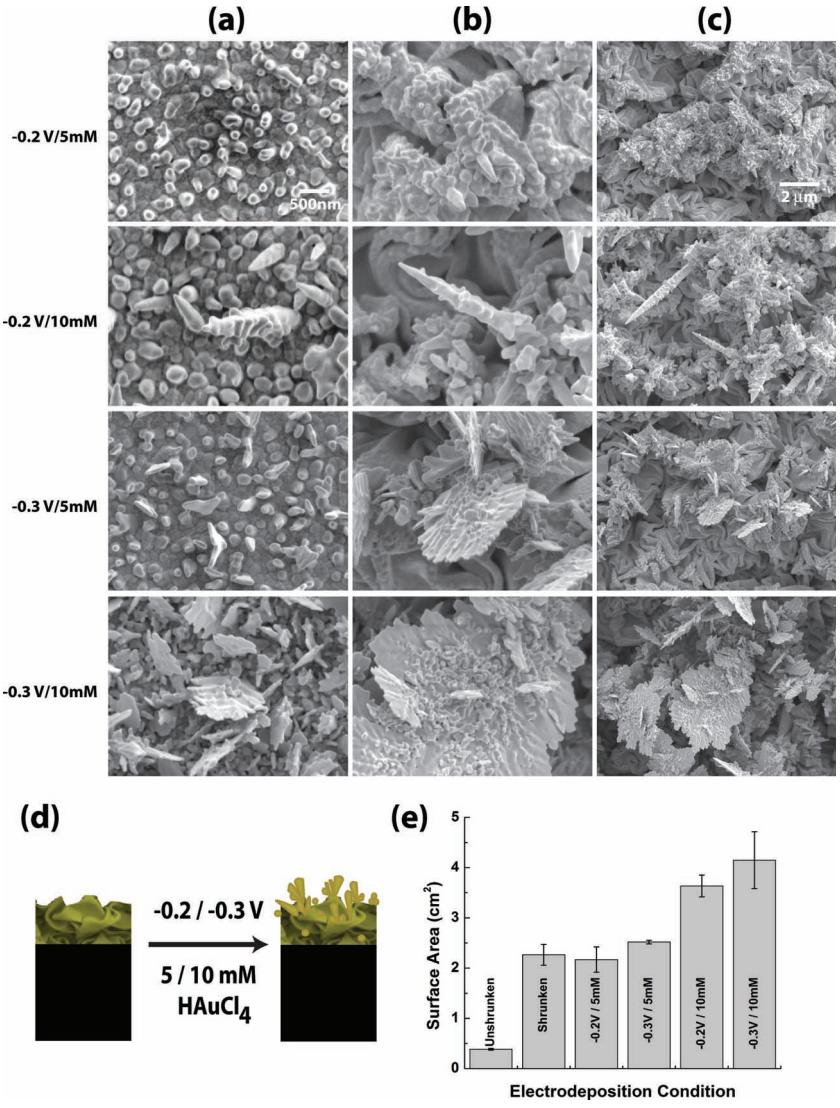

Figure 5. Electrodeposition of gold nanostructures enhances the electroactive surface area of CSEs. A comparison of SEM images of the nanostructures formed through electrodeposition on a) unshrunken flat and b,c) shrunken electrodes shows that CSEs enhance the electrodeposition process. The deposition potential and metallic salt concentration control the morphology and size of the deposited nanostructures. d) Schematic depiction of the electrodeposition process on CSEs. e) The comparison of the electroactive surface area for unshrunken, shrunken, and electrodeposited devices shows that through shrinking and electrodeposition, surface area enhancements of up to 1000% of the flat electrode can be achieved.

devices fabricated from 50 nm thick gold films. To understand the role of the micro/nanostructuring of the CSE materials on the morphology of the electrodeposited gold structures, we compared the SEM images obtained from electrodeposition experiments on un-shrunken and shrunken substrates (Figure 5a–c). Analysis of high magnification images (Figure 5b) showed that deposition on CSE devices yielded structures with similar morphology to those deposited on their unshrunken counterparts. However, the structures formed on CSE devices were significantly larger than structures formed on flat substrates under similar electrodeposition conditions. This indicates that although deposition on CSE devices does not change the electrodeposition regime, it influences the growth kinetics of the deposited structures. Local electric field enhancement[42] along with increased heterogeneous electron transfer kinetics[43,44] have been previously observed on nanostructured metallic films and are likely responsible for the enhanced deposition rate on CSE devices. The analysis of low-magnification SEM images showed that the deposition of nanostructures on CSE devices was not as homogeneous as the deposition on unshrunken devices. Under all deposition conditions, CSE substrates exhibited regions of nanostructure formation alternating with regions where no significant deposition occurred. The reasons for these differences are unclear, but might be related to the existence of regions that are inaccessible due to poor wetting of the surface by the electrolyte solution.

Nanostructures formed through electrodeposition on the electrode surfaces increased the electroactive surface area of CSE devices. This process is schematically depicted in Figure 5d. To quantify the change in surface area induced by the electrodeposited structures, we measured the charge transferred by the electrochemical formation of a monolayer of gold oxide on the modified electrodes. Figure 5e summarizes the measured electroactive surface area for devices where electrodeposition was performed under the four conditions pictured in Figure 5a–c. Significant surface area enhancement was only observed for conditions where large structures were formed, namely electrodeposition experiments conducted at 10 mM $HAuCl_4$. The largest enhancement was observed for devices where electrodeposition was performed at –0.3 V and 10 mM $HAuCl_4$, where the final electroactive surface area was ≈200% of the surface corresponding to the bare shrunken device and ≈1000% of the unshrunken device. The results presented demonstrate that it is possible to increase the electroactive surface area of CSE devices by the controlled growth of nanostructures with different morphologies through electrodeposition.

3. Conclusions

A rapid, facile and inexpensive bench-top approach has been developed for fabricating electrodes with hierarchical structures spanning from the millimeter to the nanometer range. The use of self-adhesive vinyl as masking material and a craft cutter allowed prototyping of electrodes with critical dimensions in the sub-millimeter range on timeframes of minutes to hours. Furthermore, the use of a PS shrinkable substrate allowed the reduction of the patterned feature dimensions to sub-100 μm sizes. The shrinking of the PS substrates induced stress-driven wrinkling of the gold films, and it was observed that the size of the topographical features and surface roughness could be tailored from the micrometer to the nanometer scale by adjusting the thickness of the gold film deposited. We characterized the behavior of these crumple-structured electrodes (CSEs) and found that they exhibit electrical and electrochemical properties that compare favorably with electrodes fabricated on traditional substrates such as glass. We also found that the CSEs exhibited high device-to-device reproducibility and robustness. The most attractive feature of CSEs, however, is that they exhibit significantly enhanced electroactive surface areas per geometric area (665% compared to flat electrodes). Further controllable nanostructuring was produced on CSEs through the tuned electrodeposition of gold nanostructures. We observed that the electrodeposition was improved on CSEs (compared to flat electrodes) due to the field enhancement offered by the structured surface. Devices with electrodeposited nanostructures exhibited further electroactive surface area enhancements (up to 1000% compared to flat electrodes). Thus, we have shown that it is possible to produce hierarchically structured electrodes, with features spanning the sub-millimeter to nanometer scales, through inexpensive, easy to implement and rapid bench-top techniques in timeframes less than one hour. We anticipate that such materials will find wide application in the development of highly sensitive point-of-care devices, where high surface area materials can offer enhanced signal to noise ratios and bioprocessing capability towards target analytes.

4. Experimental Section

Reagents: Potassium hexacyanoferrate(II) trihydrate ($K_4Fe(CN)_6 \cdot 3H2O$, >98.5%), potassium chloride (KCl, ≥99.0%), hydrogen tetrachloroaurate(III) trihydrate ($HAuCl_4 \cdot 3H2O$, >99.9%), hydrochloric acid (HCl ACS reagent, 37%) were purchased from Sigma-Aldrich (St. Louis, Missouri). Sulfuric acid (H_2SO_4, 98%) was purchased from Calden (Georgetown, Ontario). All reagents were of analytical grade and were used without further purification. Milli-Q grade water (18.2 MΩ) was used to prepare all solutions.

Device Fabrication: All devices were fabricated on pre-stressed polystyrene shrink films (Graphix Shrink Film, Graphix, Maple Heights, Ohio). Shrink film sheets were cleaned under orbital agitation (50 rpm) for 5 min in isopropanol, ethanol, and water baths, and were dried using a dry nitrogen stream. Self-adhesive vinyl sheets (FDC-4300, FDC graphic films, South Bend, Indiana) were laid over the cleaned shrink film sheets and evenly flattened with a hand roller. The desired gold film shapes were cut into the self-adhesive vinyl using a Robo Pro CE5000-40-CRP vinyl cutter (Graphtec America Inc., Irvine, CA) equipped with a CB09UA supersteel blade, with force, quality and speed set at 10, 1, and 1 respectively. The cut out shapes were peeled off from the shrink film using tweezers. The remaining self-adhesive vinyl was used as a mask during gold sputtering. Gold was deposited from a 99.999% purity gold target (LTS Chemical Inc., Chestnut Ridge, New York) using a Torr Compact Research Coater CRC-600 manual planar magnetron sputtering system (New Windsor, New York) onto the masked shrink film. The argon (>99.999% purity, AlphaGaz, Air Liquide, Montreal, Quebec) plasma was created by a DC current of 37 A, which allowed for a typical gold deposition rate, monitored by the quartz crystal thickness sensor, of 1.1 Å/s. The sputtered thickness of the gold was estimated according to the deposition rate and the deposition time. After sputtering the vinyl mask was removed manually using tweezers. Gold-coated shrink film devices were shrunk on aluminum boats at 130 and 160 °C in an isotemp vacuum oven (Fisher Scientific, Ottawa, Ontario). The use of an

aluminum boat as a carrier for the PS substrates provided uniform heat transfer, which ensured that there was no distortion in the shrunken devices. Self-adhesive vinyl masks were used to expose a small region of the devices used for electrochemical characterization.

SEM Characterization: SEM images of the gold films before and after shrinking were obtained using a JEOL JSM-7000S scanning electron microscope with an accelerating voltage of 3 kV, working distance of 6 mm, and low probe current.

Surface Roughness Characterization: The roughness of shrunken device surfaces was measured for gold coating thicknesses of 0, 20, 50, 100 and 200 nm using a Zygo NewView 5000 white light interferometer (Zygo Corporation, Middlefield, CT). The root mean square (RMS) and peak-to-valley (PV) values were obtained in 3–5 device areas and compared across devices. Measurements were taken with 10× and 50× interferometric objectives and both were with a 2× image zoom setting, which resulted in fields of view of 360 μm × 270 μm and 70 μm × 50 μm, respectively. Data was collected from a charge coupled device (CCD) camera with an imaging pixel size of 11.2 μm. The built in software, MetroPro, was used for data analysis. A fast fourier transform (FFT) band pass filter was applied, using cutoff frequencies of 183.35 and 558.79 mm^{-1}. Spikes with height values above 10 × RMS (root mean square) were removed from the analysis of the imaged area to eliminate any contribution from contaminants (dust particles or defects on the films) to the roughness values.

Electrochemical Characterization: Cyclic voltammetry was performed using a CHI 660D electrochemical workstation (CH Instrument, Austin, Texas) and a standard three-electrode set-up. The electrochemical system consisted of an Ag/AgCl reference electrode, a platinum wire counter electrode, and gold sputtered on polystyrene as the working electrode. To ensure that the planar geometric surface area of the working electrode was the same for samples before and after shrinking (0.25 cm^2), a vinyl mask was placed over the gold with a single 0.5 cm by 0.5 cm square cut out to expose the electrochemically active surface. To determine the electrochemically active surface area of the samples, a solution of 0.1 M H_2SO_4 was used to perform 10 CV scans at a scan rate of 0.05 V s^{-1} and a voltage range between 0 and 1.5 V. The reduction section of the resulting cyclic voltammograms were integrated using OriginPro 8 software to determine the charge and the electrochemically active surface area was calculated (surface area = charge/surface charge density) using the surface charge density of a monolayer of gold, 386 μC cm^{-2}. To test the ability to conduct electrochemical measurements, a solution of 2 mM $K_4Fe(CN)_6$ in 0.1 M KCl was used to cycle between –0.1 and 0.5 V at the following scan rates: 0.01, 0.02, 0.04, and 0.08 V s^{-1}. Also, chronoamperometry was performed using solutions ranging from 50 μM to 100 mM $K_4Fe(CN)_6$ in 1 M KCl at a potential of 0.5 V for 1 s.

Electrical Characterization: Sheet resistance (R_s) measurements were taken using the HL5500PC- Hall effect measurement system with a HL5500 buffer amplifier (Nanometrics, Milpitas, California). Four gold probe tips were used to take R_s measurements of the samples in a standard van der Pauw configuration. The sheet resistance was calculated according to:

$$R_s = \frac{2.2662\,(V_{43} + V_{23})}{I} \times F \times Q \quad (1)$$

where I is the applied current, V_{43} and V_{23} are the potentials measured perpendicular to each other on the film in response to the current, Q is the symmetry factor and is calculated by $Q = \frac{V_{43}}{V_{23}}$, and F is a correction factor for any asymmetry and is calculated by: $F = 1 - 0.34657A - 0.09236A^2$, where $A = \left[\frac{Q-1}{Q+1}\right]^2$. In order to cancel thermoelectric and other effects, the currents were applied in both directions between two tips, and then the measured potentials were averaged.

Electrodeposition: The CHI 660D Electrochemical Workstation (CH Instrument, Austin, Texas) was used for electrodeposition with the standard three-electrode set-up described above. To ensure the planar geometric surface area of the working electrode was the same for samples before and after shrinking (0.25 cm^2), a vinyl mask was placed over the gold with a single 0.5 cm by 0.5 cm square cut out to expose the electrochemically active surface. Gold nanostructures were grown by electrodeposition on the gold-polystyrene substrate using solutions containing 5 and 10 mM $HAuCl_4$ in 0.5 M HCl at potentials of –0.2 or –0.3 V for 900 s.

Supporting Information

Supporting Information is available from the Wiley Online Library or from the author.

Acknowledgements

The authors thank Laura Dodge for help with the measurement of contact angles and Dr. Maneesh Khanna for help with white light interferometry. This research made use of facilities at the McMaster Manufacturing Research Institute. J.M.M.-M. acknowledges funding through the Science and Engineering Research Board at McMaster University.

Received: November 2, 2012
Revised: November 30, 2012
Published online: January 17, 2013

[1] R. Lakes, *Nature* **1993**, *361*, 511.
[2] P. Fratzl, R. Weinkamer, *Prog. Mater. Sci.* **2007**, *52*, 1263.
[3] L. Tsakalakos, J. Balch, J. Fronheiser, B. A. Korevaar, O. Sulima, J. Rand, *Appl. Phys. Lett.* **2007**, *91*, 233117.
[4] M. J. Bierman, S. Jin, *Energy Environ. Sci.* **2009**, *2*, 1050.
[5] A. Chen, D. K. Lieu, L. Freschauf, V. Lew, H. Sharma, J. Wang, D. Nguyen, I. Karakikes, R. J. Hajjar, A. Gopinathan, E. Botvinick, C. C. Fowlkes, R. A. Li, M. Khine, *Adv. Mater.* **2011**, *23*, 5785.
[6] M. J. Dalby, N. Gadegaard, R. Tare, A. Andar, M. O. Riehle, P. Herzyk, C. D. W. Wilkinson, R. O. C. Oreffo, *Nat. Mater.* **2007**, *6*, 997.
[7] M. M. Stevens, J. H. George, *Science* **2005**, *310*, 1135.
[8] J. M. J. Fréchet, *J. Polym. Sci. Part A: Polym. Chem.* **2003**, *41*, 3713.
[9] M. Goldberg, R. Langer, X. Jia, *J. Biomater. Sci., Polym. Ed.* **2007**, *18*, 241.
[10] L. Soleymani, Z. Fang, E. H. Sargent, S. O. Kelley, *Nat. Nanotechnol.* **2009**, *4*, 844.
[11] L. Soleymani, Z. Fang, B. Lam, X. Bin, E. Vasilyeva, A. J. Ross, E. H. Sargent, S. O. Kelley, *ACS Nano* **2011**, *5*, 3360.
[12] X. Lu, Y. Xiao, Z. Lei, J. Chen, *Biosens. Bioelectron.* **2009**, *25*, 244.
[13] Z. Wen, S. Ci, J. Li, *J. Phys. Chem. C* **2009**, *113*, 13482.
[14] Y. Luo, V. Misra, *Nanotechnology* **2006**, *17*, 4909.
[15] H. Duan, J. Zhao, Y. Zhang, E. Xie, L. Han, *Nanotechnology* **2009**, *20*, 135306.
[16] R. Inguanta, S. Piazza, C. Sunseri, *Nanotechnology* **2007**, *18*, 485605.
[17] Y. Xia, G. M. Whitesides, *Annu. Rev. Mater. Sci.* **1998**, *28*, 153.
[18] C.-C. Fu, A. Grimes, M. Long, C. G. L. Ferri, B. D. Rich, S. Ghosh, S. Ghosh, L. P. Lee, A. Gopinathan, M. Khine, *Adv. Mater.* **2009**, *21*, 4472.
[19] D. Nguyen, D. Taylor, K. Qian, N. Norouzi, J. Rasmussen, S. Botzet, M. Lehmann, K. Halverson, M. Khine, *Lab Chip* **2010**, *10*, 1623.
[20] A. Grimes, D. N. Breslauer, M. Long, J. Pegan, L. P. Lee, M. Khine, *Lab Chip* **2008**, *8*, 170.
[21] W. M. Haynes, *CRC handbook of chemistry and physics*, CRC; Taylor & Francis, Boca Raton, FL **2011**.
[22] D. Taylor, D. Dyer, V. Lew, M. Khine, *Lab Chip* **2010**, *10*, 2472.
[23] X. M. Zhao, Y. Xia, O. J. A. Schueller, D. Qin, G. M. Whitesides, *Sens. Actuators A* **1998**, *65*, 209.

[24] C.-C. Fu, A. Grimes, M. Long, C. G. L. Ferri, B. D. Rich, S. Ghosh, S. Ghosh, L. P. Lee, A. Gopinathan, M. Khine, *Adv. Mater.* **2009**, *21*, 4472.
[25] Y. Shao, M. A. Brook, *J. Mater. Chem.* **2010**, *20*, 8548.
[26] C. M. Stafford, C. Harrison, K. L. Beers, A. Karim, E. J. Amis, M. R. VanLandingham, H.-C. Kim, W. Volksen, R. D. Miller, E. E. Simonyi, *Nat. Mater.* **2004**, *3*, 545.
[27] P. Yoo, H. Lee, *Phys. Rev. Lett.* **2003**, *91*, 154502.
[28] P. Yoo, K. Suh, H. Kang, H. Lee, *Phys. Rev. Lett.* **2004**, *93*, 034301.
[29] J. S. Sharp, D. Vader, J. A. Forrest, M. I. Smith, M. Khomenko, K. Dalnoki-Veress, *Eur. Phys. J. E* **2006**, *19*, 423.
[30] C.-C. Fu, G. Ossato, M. Long, M. A. Digman, A. Gopinathan, L. P. Lee, E. Gratton, M. Khine, *Appl. Phys. Lett.* **2010**, *97*, 203101.
[31] J. Groenewold, *Phys. A* **2001**, *298*, 32.
[32] Z. Huang, W. Hong, Z. Suo, *Phys. Rev. E* **2004**, *70*, 030601.
[33] J. Y. Chung, A. J. Nolte, C. M. Stafford, *Adv. Mater.* **2011**, *23*, 349.
[34] A. Shahraz, A. Borhan, K. A. Fichthorn, *Langmuir* **2012**, *28*, 14227.
[35] M.-C. Choi, Y. Kim, C.-S. Ha, *Prog. Polym. Sci.* **2008**, *33*, 581.
[36] M. C. McAlpine, H. Ahmad, D. Wang, J. R. Heath, *Nat. Mater.* **2007**, *6*, 379.
[37] T. Söderström, F.-J. Haug, V. Terrazzoni-Daudrix, C. Ballif, *J. Appl. Phys.* **2008**, *103*, 114509.
[38] H. K. Chae, D. Y. Siberio-Pérez, J. Kim, Y. Go, M. Eddaoudi, A. J. Matzger, M. O'Keeffe, O. M. Yaghi, *Nature* **2004**, *427*, 523.
[39] Y. Li, Z.-Y. Fu, B.-L. Su, *Adv. Funct. Mater.* **2012**, *22*, 4634.
[40] A. J. Bard, L. R. Faulkner, *Electrochemical methods: fundamentals and applications*, Wiley, New York **2001**.
[41] W. R. Osório, L. C. Peixoto, M. V. Canté, A. Garcia, *Electrochim. Acta* **2010**, *55*, 4078.
[42] S. Sriram, M. Bhaskaran, R. Ahluwalia, T. G. Nguyen, N. Ng, D. J. Srolovitz, K. Kalantar-zadeh, A. Mitchell, *ACS Nano* **2011**, *5*, 1067.
[43] H.-Y. Gu, A.-M. Yu, H.-Y. Chen, *J. Electroanal. Chem.* **2001**, *516*, 119.
[44] S. Bharathi, M. Nogami, S. Ikeda, *Langmuir* **2001**, *17*, 1.